How to Improve the Ductility of Nanostructured Materials

J. Eckert[a,]*, C. Duhamel[a,b], J. Das[a], S. Scudino[a], Z. F. Zhang[c] and K. B. Kim[d]

[a]*IFW Dresden, Institut für Festkörperanalytik und Strukturforschung,*
Postfach 27 01 16, D-01171 Dresden, Germany
[b]*FG Physikalische Metallkunde, FB 11 Material- und Geowissenschaften,*
Technische Universität Darmstadt, Petersenstrasse 23, D-64287 Darmstadt, Germany
[c]*Shenyang National Laboratory for Materials Science, Institute of Metal Research,*
Chinese Academy of Sciences, 72 Wenhua Road, Shenyang 110016, P.R. China
[d]*Department of Advanced Materials Engineering, Sejong University,*
98 Gunja-dong, Gwangjin-gu, Seoul 143-747, Korea

Abstract Nanostructured materials exhibit attractive mechanical properties that are often superior to the performance of their coarse-grained counterparts. However, one major drawback is their low ductility, which limits their potential applications. In this paper, different strategies to obtain both high strength and enhanced ductility in nanostructured materials are reported for Ti-base and Zr-base alloys. The first approach consists of designing an *in-situ* composite microstructure containing ductile bcc or hcp dendrites that are homogeneously dispersed in a nanostructured matrix. The second approach is related to refining the eutectic structure of a Ti-Fe-Sn alloy. For all these materials, the microstructure, mechanical properties, deformation and fracture mechanisms will be discussed.

Keywords : Nanostructured materials, Ti-base, Zr-base alloys, Ti-Fe-Sn alloy

1. Introduction

In the past decades, the development of bulk metallic glasses and nanostructured materials with high strength, high hardness and unique chemical and physical properties has opened new perspectives for advanced structural and functional materials[1-3]. Unfortunately, the ductility of these materials is disappointingly low compared to their coarse-grained counterparts, which limits their potential application[4]. Different factors have been reported to be responsible for this low plastic deformability[5]. On one hand, fully dense samples with a nanometer-sized structure are difficult to process and the residual porosity is usually detrimental to plastic deformation, especially in tension[4]. On the other hand,

nanocrystalline materials are prone to plastic instabilities and their deformation behavior is usually characterized by the absence of strain hardening[6]. Localization of the deformation, either via shear banding[7] or necking[8] in tension, leads to failure of the materials in the early stage of plastic deformation.

In order to improve the ductility of nanostructured materials without sacrificing their high strength, several strategies have been attempted, which can be classified as follows[9]: (i) optimization of the existing materials, (ii) design of new architectures. For the first approach, the idea is mainly to improve the strain hardening and the strain-rate hardening either by significantly decreasing the temperature to decrease dynamic recovery[10] or by enhancing the

*Corresponding Author : [Tel : +49-351-4659-602; E-mail : j.eckert@ifw-dresden.de]

strain-rate sensitivity[11]. The second approach considers creating composite materials where one "phase" provides the ductility and another one the strength. This can be done by reinforcing the matrix with nanoparticles and nanoprecipitates[12,13], by preparing homogeneous structures with a bimodal grain size distribution[14,15] or through heterogeneous structures with different phases and/or different length scales[16,17].

Based on this idea and on the encouraging results obtained on similar microstructures with a glassy matrix[18-20], the preparation of an *in-situ* composite microstructure consisting of ductile dendrites embedded in a nanostructured matrix has been performed. This article reports on the microstructure, mechanical properties and deformation mechanisms of nanostructured Ti-base and Zr-base alloys containing a ductile bcc dendritic phase. The possibility to use a different ductile hcp dendritic phase is discussed through the example of a $Zr_{74.9}Ti_{10.5}Ni_{14.6}$ alloy. In an attempt to obtain both high strength and enhanced ductility without the help of any additional phase, the formation and deformation behavior of Ti-base ultrafine eutectic structures is also presented.

2. Nanostructured Matrix with Ductile Bcc Dendrites

2.1. Alloy design

Generally, bulk metallic glasses are obtained for compositions close to a deep eutectic and for sufficiently high cooling rate. By addition of the proper elements to the glass-forming composition and/or by changing the solidification conditions, a wide variety of microstructures have been reported for Zr-base and Ti-base alloys[21,22]. The compositions of the Ti-base and Zr-base alloys discussed in this section were designed by modification of glass-forming composition, considering a pseudo-ternary phase diagram consisting of (i) the main element (Ti or Zr), (ii) bcc-β-phase formers and stabilizers (Nb, Ta, Mo) and (iii) eutectic matrix formers (Cu, Ni, Al).

2.2. Microstructure

A representative microstructure of a nanostructured matrix/dendrites composite is presented in Fig. 1 for an arc-melted $Ti_{60}Cu_{14}Ni_{12}Sn_4Nb_{10}$ alloy[23]. The scanning electron microscopy (SEM) backscattered
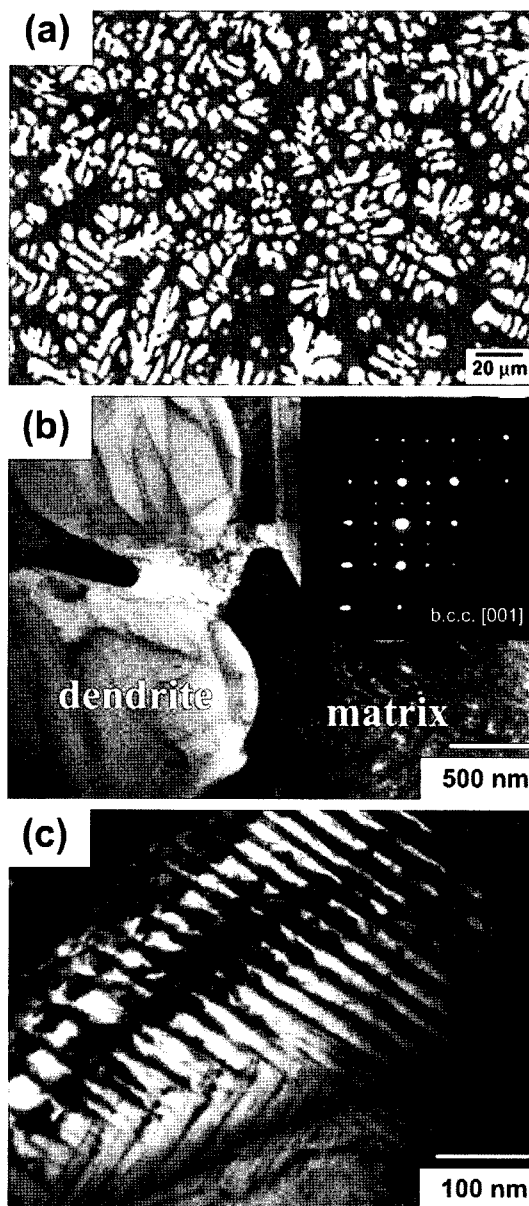

Fig. 1. Microstructure of the as-melted $Ti_{60}Cu_{14}Ni_{12}Sn_4Nb_{10}$ alloy: SEM backscattered electron image (a), bright-field image of the microstructure (b) and of the eutectic matrix (c). The inset in (b) displays the selected area diffraction pattern taken from the dendrites.

electron micrograph (Fig. 1(a)) shows micrometer-size dendrites (bright phase) homogeneously embedded in a nanostructured matrix (dark phase). The volume fraction of the dendrites is about 40 vol.%. The dendritic phase has a "lopstick-like" morphology and consists of a (bcc)-β-Ti-solid solution (diffraction pattern in Fig. 1(b)). Energy dispersive X-ray (EDX) analysis reveals that they are enriched in Ta and Sn compared to the nominal composition. The matrix contains regions with different compositions, as shown by the gray and dark contrast in the SEM micrograph (Fig. 1(a)). The gray area is mostly enriched in Ni whereas the dark area is mostly enriched in Cu. Transmission electron microscopy (TEM) investigations show that the matrix exhibits a binary nanoscale eutectic structure with a layer thickness of 50-150 nm (Figs. 1(b) and (c)). For the matrix bcc-β-Ti and α-Ti structures are ·found as well as the Ti_2Cu and Ti_2Ni intermetallics.

2.2.1. Influence of the composition

The final microstructure of the dendrite-reinforced nanostructured alloys strongly depends on the alloy composition[23,24]. As mentioned in section II.1., composite microstructures with a dendritic phase are usually obtained in pseudo-ternary systems[21]. Elements such as Nb or Sn, which have similar bcc structures and similar atomic radii as Ti[21], are good β-phase stabilizers and enhance the formation of the dendritic phase. On the contrary, elements like Cu or Ni, which have a fcc structure and smaller atomic radii as Ti[21], will act the reverse way. The final microstructure, thus, results from a balance between the b-phase formers content (Nb + Sn) and the eutectic matrix formers content (Cu + Ni). The higher the (Nb + Sn) content is, the larger is the volume fraction of the dendrites and the coarser are the grains in the matrix, as shown in Fig. 2. Moreover, changes in the nominal composition induce changes in the local composition, which, in turn, modifies the morphology of the dendrites from an orientated to a more equiaxed shape. At last, high (Cu+Ni) contents
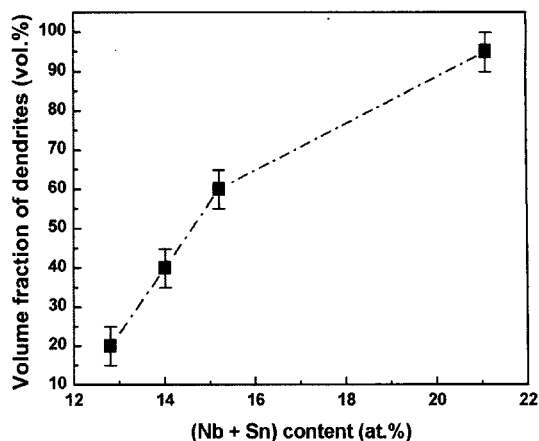

Fig. 2. Variation of the volume fraction of the dendrites and of the grain size of the matrix with the (Nb + Sn) content.

enhance the formation of the intermetallic phases in the matrix. The more complex structure of the matrix is supposed to favor the precipitation of finer grains[21].

2.2.2. Influence of the casting method

The influence of the casting conditions on the final microstructure was studied for a $Zr_{73.5}Nb_9Cu_7Ni_1Al_{9.5}$ alloy[25]. Three different casting methods, corresponding to different cooling rates, were used: suction casting, centrifugal casting and cold-crucible casting. In all the cases, the as-cast microstructure exhibits a bcc-β-Zr dendritic phase embedded in an interdendritic matrix consisting of nano/ultrafine $CuZr_2$-type phase crystals dispersed in an amorphous matrix. The estimated cooling rate as well as the cell size of the dendrites, their arms spacing and the matrix grain size of the as-cast alloys are reported in Table 1 for each process. The finer microstructure is obtained for the suction cast alloy for which the solidification has been faster[25]. When decreasing the solidification rate, more dendrites exhibiting a more equiaxed shape are formed. The dendrites cell size does not seem to be affected by the process contrary to the secondary arms spacing, which becomes larger. At last, the casting method has a strong effect on the matrix grain size as a faster

Table 1. Effect of the casting method and of the associated cooling rate on the dendrites cell size and arm spacing and on the grain size of the matrix for as-cast $Zr_{73.5}Nb_9Cu_7Ni_1Al_{9.5}$ composite alloys.

Casting method	Cooling rate (K.s^{-1})	Dendrites size (μm)	Arm spacing (nm)	Matrix grain size (nm)
suction	200 – 2000	25 ± 5	1.45 – 3.42	2.3 – 50
centrifugal	175 – 750	30 ± 5	2.2 – 3.48	30 – 200
cold-crucible	40 – 180	25 ± 5	3.52 – 5.5	200 – 400

solidification leads to a finer grain size.

2.3. Mechanical properties

Fig. 3 shows the variation of yield strength (σ_y) and plastic deformation (ε_p) with the volume fraction of the dendrites for as-melted Ti-Cu-Ni-Sn-Nb alloys with different Nb contents and for $Zr_{73.5}Nb_9Cu_7Ni_1Al_{9.5}$ alloys cast using different methods. All samples combine a high strength ($\sigma_y \geq 1$ GPa) and substantial plastic deformation ($\varepsilon_p \geq 9\%$) except for the Zr-base specimens with lower amount of dendrites (70-90 vol.%). It can be clearly seen that higher volume fractions of the dendritic phase (90 vol.%) enhance the plastic deformability but decrease the yield strength of the composite. For example, for the Ti-base alloys, by increasing the volume fraction of the dendrites from 20 to 40 vol.%, the yield strength decrease from 1313 MPa to 1052 MPa while the plastic deformation increases from 8.9% to 21%. The same trend is observed for the Zr-base alloys where an increase from 70 to 95 vol.% of the volume fraction of the dendrites leads to a decrease of the yield strength from 1555 MPa to 1231 MPa but an increase of the plastic deformation from 2.1% to 15.8%.

The mechanical properties are closely linked to the obtained microstructure. The deformation behavior of the composite results from a combination of the intrinsic behavior of each phase. The ductile dendrites contribute to the overall plastic deformation whereas the nanostructured matrix contributes to the strength. Therefore, the decrease in the yield strength with increasing volume fraction of dendrites can be attributed to the combined effect of the lower volume fraction of the matrix, the lower amount (or even the absence) of the intermetallic phases and the larger grain size. On the contrary, the enhanced ductility results from the high volume fraction of the dendrites and, to a lower extent, to the decreasing detrimental effect of the matrix.

3. Composite with Ductile Hcp Dendrites

3.1. Microstructure

The first prepared nanostructured matrix/dendrites composites displayed a ductile phase with a bcc structure[16,26]. In an attempt to examine the possibility to use a different ductile dendritic phase, with a hexagonal structure, a $Zr_{74.9}Ti_{10.5}Ni_{14.6}$ alloy has been developed[27]. The as-cast microstructure, shown in Fig. 4(a), reveals a homogeneous distribution of dendrites (bright contrast) embedded in a complex interdendritic matrix (gray and black contrasts). The two different contrasts in the matrix suggest the coexistence of two phases with different compositions.
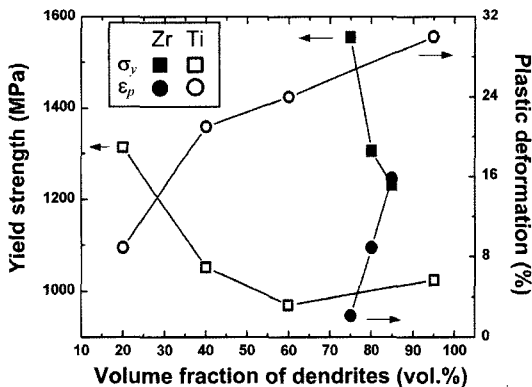

Fig. 3. Evolution of yield strength σ_y (□, ■) and plastic deformation ε_p (○, ●) with the volume fraction of the dendrites for two series of Ti-Cu-Ni-Sn-Nb (□, ○) and $Zr_{73.5}Nb_9Cu_7Ni_1Al_{9.5}$ (■, ●) alloys.
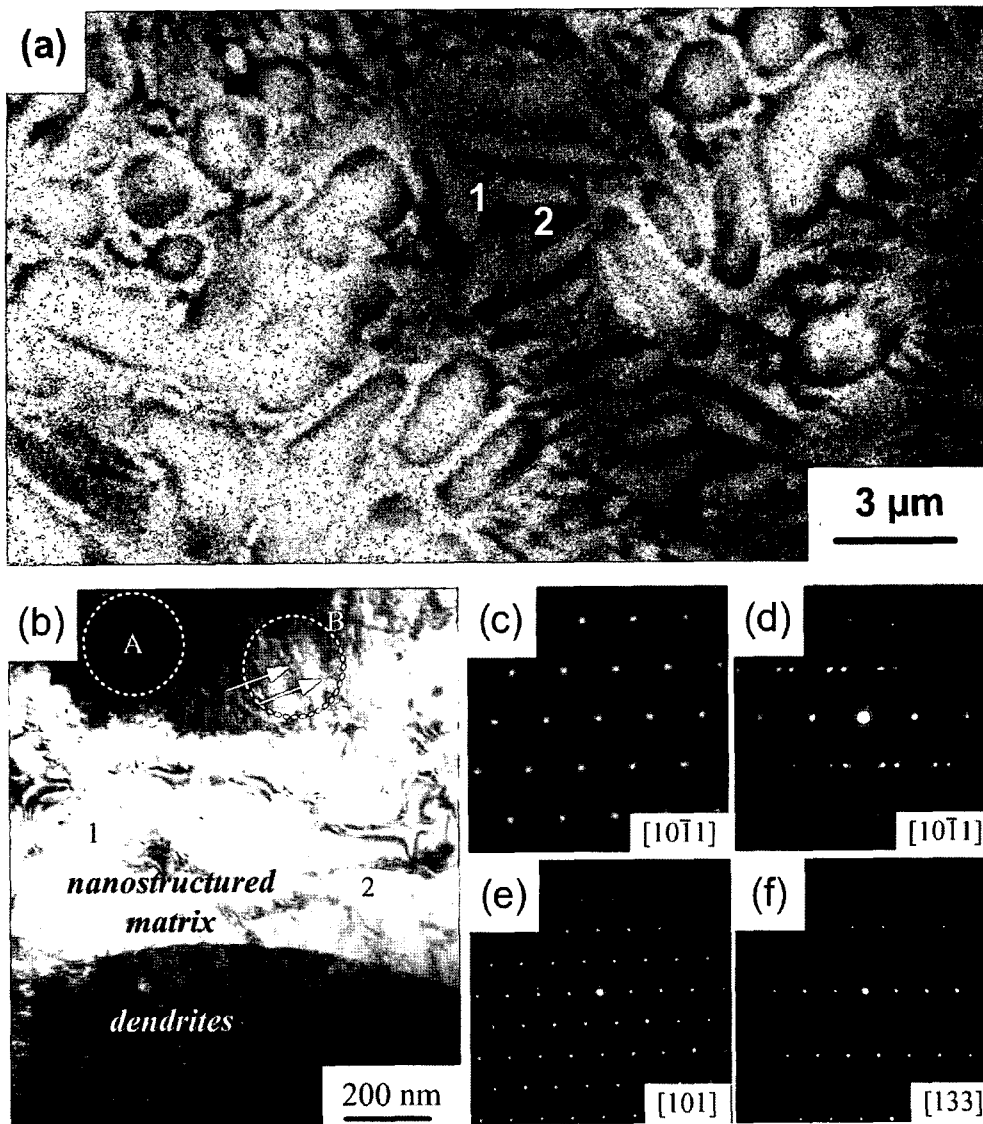
Fig. 4. SEM backscattered electron image (a) and TEM bright field image (b) of the as-cast $Zr_{74.9}Ti_{10.5}Ni_{14.6}$ alloy; (c) and (d), selected area diffraction pattern corresponding to the dendrites (zones A and B in (b)); (e) and (f), selected area diffraction pattern corresponding to the matrix (grains 1 and 2 in (c)).

EDX analysis reveals that the composition of the dendrites is $Zr_{87}Ti_{10}Ni_3$ and confirms that the matrix consists of two phases of composition $Zr_{70}Ti_9Ni_{21}$ (region 1) and $Zr_{55}Ti_{23}Ni_{22}$ (region 2). In order to identify the phases, TEM investigations were performed (Figs. 4(b-d)). The bright field image in Fig. 4(b) shows the micrometer-scale size of the dendrites dispersed in a bimodal nanostructured matrix. The size of the grains with a mottled contrast (like grain 1) is about 200~300 nm while the size of the grains with a bright contrast (like grain 2) is in the range of 50 to 100 nm. Selected area diffraction pattern (SADP) of different areas of the microstructure are shown in Figs. 4(c-f). The dendrites have the hexagonal structure of an a-Zr solid solution (Fig. 4(c)). Close to the interface with the matrix (region B in Fig. 4(b)), the presence of twins is detected, as revealed by the SADP in Fig. 4(d). The SADP in
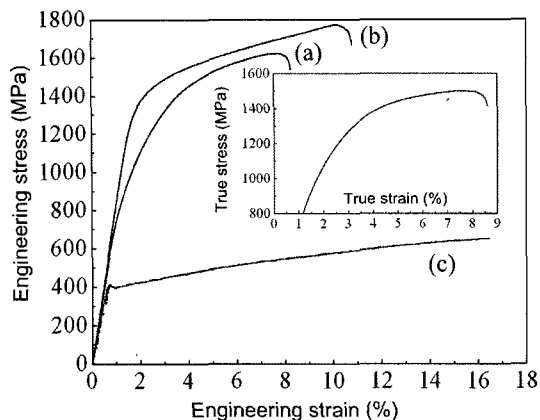
Fig. 5. Room temperature stress-strain curves of the as-cast $Zr_{74.9}Ti_{10.5}Ni_{14.6}$ alloy (a), a $Zr_{73.5}Nb_9Cu_7Ni_1Al_{9.5}$ alloy with bcc dendrites (b), a conventional a-Zr alloy (c). The inset shows the true stress-strain curve for the $Zr_{74.9}Ti_{10.5}Ni_{14.6}$ alloy.

Fig. 4(e) and Fig. 4(f) show that the matrix contains a hexagonal $MgZn_2$-type phase (grain 1) and the tetragonal Zr_2Ni phase (grain 2).

3.2. Mechanical properties

The room temperature stress-strain curve of the $Zr_{74.9}Ti_{10.5}Ni_{14.6}$ composite is shown in Fig. 5(a). The sample exhibits a remarkable deformation behavior with a high strength and significant plastic deformation. After yielding at $\sigma_y = 870$ MPa, the stress continuously increses with further deformation up to 1622 MPa leading to pronounced work hardening. Failure occurs after 7.6 % total strain. This behavior is comparable to the one obtained for a $Zr_{73.5}Nb_9Cu_7Ni_1Al_{9.5}$ alloy containing bcc dendrites (Fig. 5(b)), even though slightly higher stress (from 1400 to 2000 MPa) and ductility (up to 17.5%) can be reached in the latter case. Moreover, although the plastic strain is reduced, the maximum stress reached for the Zr-Ni-Ti composite is twice higher than the one obtained for conventional α-Zr alloys (Fig. 5(c)).

4. Simple Nanoeutectic Structure

4.1. Microstructure

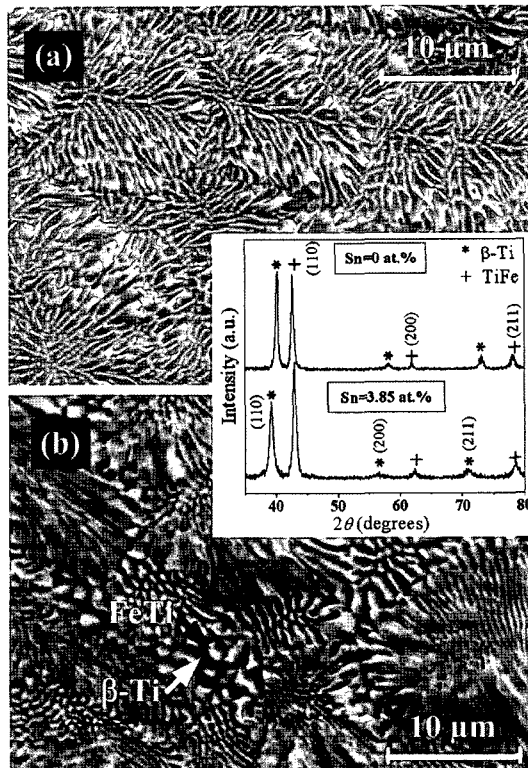In an attempt to develop high strength Ti-base alloys

Fig. 6. SEM micrograph of the as-cast $Ti_{70.5}Fe_{29.5}$ (a) and $Ti_{67.79}Fe_{28.36}Sn_{3.85}$ (b) alloys. The inset shows the XRD patterns of the two alloys.

with an enhanced ductility, the preparation of ultrafine eutectic structures was performed[28]. $Ti_{70.5}Fe_{29.5}$ and $Ti_{67.79}Fe_{28.36}Sn_{3.85}$ rods were prepared from arc-melted master alloys by levitation melting and subsequent casting in a cold-crucible device. The XRD diffraction patterns (Fig. 6) of the two as-prepared alloys reveal the coexistence of a bcc β-Ti solid solution (A2) with a FeTi (B2) phase. The volume fractions of the A2 and B2 phases are 79 vol.% and 21 vol.% for $Ti_{70.5}Fe_{29.5}$ and 64 vol.% and 36 vol.% for $Ti_{67.79}Fe_{28.36}Sn_{3.85}$. The microstructure of both alloys consists of an ultrafine eutectic, as shown in Figs. 6(a) and (b). The binary alloy exhibits homogeneously distributed equiaxed eutectic colonies with a cell size of 20 ± 5 μm and an eutectic rod spacing of 525 nm. The bright contrast corresponds to the FeTi phase and the dark contrast to the β-Ti solid solution. Oval-shaped eutectic colonies with pronounced

boundaries and a cell size of 50-10 μm are observed for the ternary alloy. The growth of the Fe-Ti phase is parallel at the center of the colony but becomes restricted and coarser in the longitudinal direction close to the colony boundaries. The interlamellar spacing is 300 nm. X-ray diffraction (XRD) and EDX analyses reveal a supersaturation of β-Ti in the binary alloy, with 22.3 at.% Fe instead of 15 at.% for the equilibrium phase[28]. In the ternary alloy, a limited solubility of Sn in the FeTi phase ($Ti_{52.5}Fe_{46.8}Sn_{0.7}$) and substitution of Fe by Sn in the β-Ti solid solution ($Ti_{82.3}Fe_{9.2}Sn_{8.5}$) are observed.

4.2. Mechanical properties

The engineering stress-strain curves of the two alloys are reported in Fig. 7. The binary alloy exhibits high yield strength and maximum stress of 1885 MPa and 1935 MPa, respectively, but a limited ductility with a total strain of 2.6%. High yield strength (σ_y = 1794 MPa), high maximum strength (σ_m = 2260 MPa) and substantially enhanced total deformation (ε_ϕ = 9.6%) are obtained for the ternary alloy. This combination of strength and ductility is significantly improved compared to the dendritic phase reinforced composite alloys for which the yield strength is usually in the range of 1000~1400 MPa. The improvement of the mechanical properties for the $Ti_{67.79}Fe_{28.36}Sn_{3.85}$ alloy is believed to come from the addition of Sn, which modifies the shape, the

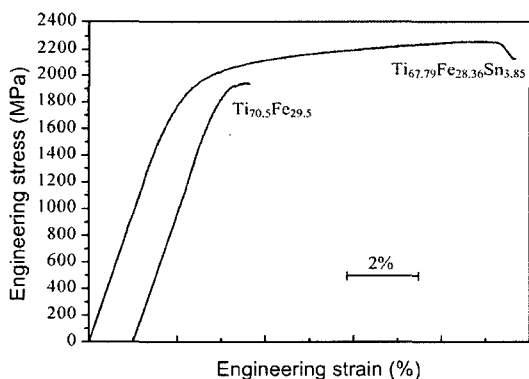Fig. 7. Room temperature engineering stress-strain curves of the $Ti_{70.5}Fe_{29.5}$ and the $Ti_{67.79}Fe_{28.36}Sn_{3.85}$ alloys.

size and, above all, the chemical composition of the eutectic phases. In particular, the limited solubility of Fe in the β-Ti solid solution is supposed to have great importance for improving the deformation behavior[28].

5. Deformation and Fracture Mechanisms

5.1. Nanostructured matrix/dendrite composites

The fracture surface and the surface of the deformed samples were widely investigated for Ti-base composites[23,29-31]. In this section, we will concentrate on the fractographic features of the $Ti_{66.1}Cu_8Ni_{4.8}Sn_{7.2}Nb_{13.9}$ alloy. As for most of the nanostructured matrix/dendrites composites, failure follows a shear mode, as shown in Fig. 8(a). The fracture angle is equal to 51°. It increases from 46° to 51° when increasing the Nb content of a Ti-Cu-Ni-Sn-Nb alloy from 8 to 14 at.%. This indicates that the fracture of these composites does not follow the Mohr-Coulomb criterion, which is usually suitable to describe shear fracture[32]. An example of the surface of the $Ti_{66.1}Cu_8Ni_{4.8}Sn_{7.2}Nb_{13.9}$ alloy after failure at a compressive strain of 30% is shown in Fig. 8(b). Dense shear bands are formed in two directions. Primary shear bands (p.s.b.), parallel to the fracture plane, develop at the first stage of plastic deformation. With further deformation, secondary shear bands (s.s.b.), perpendicular to the previous ones, are activated[33] All the shear bands exhibit a bent morphology, probably due to the high compressive strain[33]. Bending of the shear bands and anomalously high fracture angles are attributed to the high compressive strain according to the following mechanism[21,31]. At the early stage of deformation, a primary shear band is activated, forming a angle $\theta_c^0 \approx 45°$ with the loading axis. With higher compressive strains, secondary shear bands are initiated, which interact with the primary shear band. The strong shear deformation leads to a strong impingement of the two sets of shear bands resulting in the
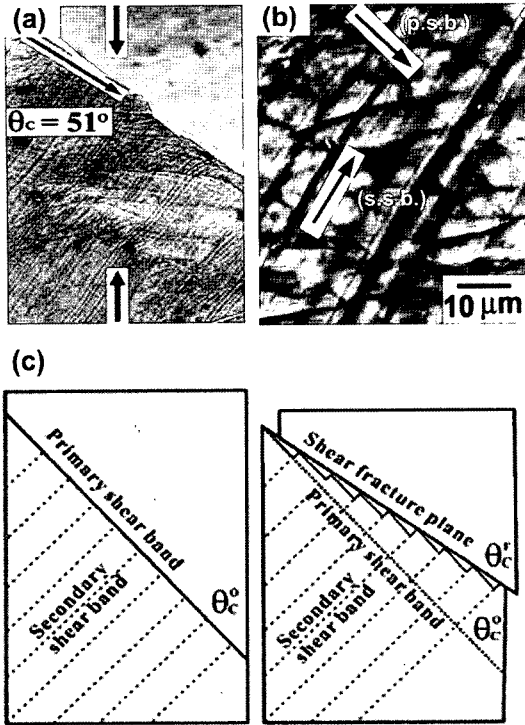
Fig. 8. Fracture geometry (a) and surface (b) of the fractured $Ti_{66.1}Cu_8Ni_{4.8}Sn_{7.2}Nb_{13.9}$ alloy, (c) illustration of the rotation mechanism of the shear fracture.
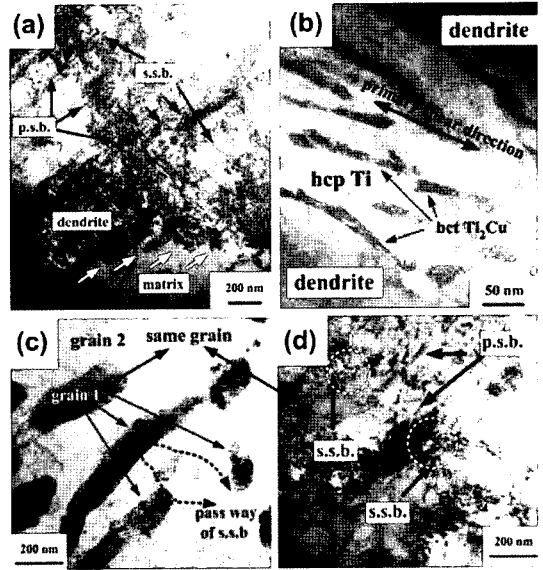

Fig. 9. TEM bright-field images of (a) and (b) the dendrite-matrix interface and (c) and (d) the nanostructured matrix of the $Ti_{66.1}Cu_8Ni_{4.8}Sn_{7.2}Nb_{13.9}$ deformed alloy.

formation of steps on one of the shear planes. The macroscopic shear plane, joining all the steps, is thus rotated compared to the plane of the initial primary shear band and makes an angle θ_c^0 with the loading axis. During deformation, both the volume V and the length l_{SB} of the primary shear band do not change. Consequently:

$$V = a_0 \times a_0 \times l_0 = a \times a \times 1 \quad \text{and} \quad (1a)$$

$$l_{SB} = a_0/\sin\theta_C^0 = a/\sin\theta_C^F \quad (1b)$$

where a_0, l_0 and a, 1 are the initial and final dimensions of the sample, respectively.

In compression, the plastic strain ε_p is given by

$$\varepsilon_p = (l_0 - 1)/l_0 \quad (2)$$

From the previous relationships, one finds:

$$\sin(\theta_C^0) = \sqrt{(1-\varepsilon_p)}\sin(\theta_C^F) \quad (3)$$

This indicates that (i) the fracture angle θ_C^F is higher than the initial shear plane angle θ_C^0, and (ii) the fracture angle increases with plastic deformation, which is consistent with the experimental results[31].

Further investigations on the microscopic mechanisms occurring during the plastic deformation of the composite microstructure were carried out using TEM[34,35]. For this purpose, a $Ti_{66.1}Cu_8Ni_{4.8}Sn_{7.2}Nb_{13.9}$ sample was deformed up to a total strain of 25%, i.e. before failure. Fig. 9(a) shows the presence of multiple shear bands, which are organized in two perpendicular networks. Because they are initiated first, the primary shear bands (p.s.b.) are more strained than the secondary shear bands (s.s.b.) and appear on the bright field image with a higher contrast. The spacing between the p.s.b. is in the range 150 to 250 nm. As can be seen in Fig. 9(a), most of the p.s.b. pass through the dendrite without being interrupted by the s.s.b. However, the intersection of one of the p.s.b. with s.s.b. leaves a step interface between the dendrite and the nanostructured matrix. The step interfaces, with a distance of 80 to 200 nm, enable to accommodate the shear strain. Other interfaces

between the dendrites and the matrix are shown in Fig. 9(b). The interfaces are parallel to the propagation of the p.s.b. and no steps are formed. The shear band propagation inside the nanostructured matrix is shown in Figs. 9(c) and 9(d). The two bright field images correspond to the same area of the matrix but the micrograph 9(d) was obtained by tilting the sample by 9°. The grains are elongated in the direction of the p.s.b. with a width of 100-160 nm and a length of 200-800 nm. The p.s.b. pass through the boundaries of the elongated grains while the s.s.b., perpendicular to the p.s.b. direction, are deflected by the grain marked 1. They are no more visible between point 1 and point 2 in Fig. 9(c) and appear again after point 2. Point 1 corresponds to the boundary between the hcp a-Ti phase (grain 2) and the Ti_2Cu phase (grain 1). This latter phase is much harder than the hcp α-Ti phase[36]. This suggests that the s.s.b. cannot cut through the Ti_2Cu phase and therefore are deflected in the nanostructured matrix.

From the above observations, one can deduce that the mechanical behavior of the nanostructured matrix/dendrites composites results from a balance between the contribution of both the dendritic phase and the nanostructured matrix and strongly depends on the interaction between these two different contributions. The dendrites constitute the ductile phase and provide ductility to the alloy whereas the matrix constitutes the hard phase and provides the strength via the grain size and the chemical nature of its crystallites. The deformation mechanism of such a composite structure can be described as follows. During deformation, when the yield strength is reached, primary shear bands are initiated inside the matrix. The dendrites act as obstacles to their propagation. In order to accommodate the stress due to the interaction between the dendritic phase and the primary shear bands, secondary shear bands are formed perpendicularly to the primary shear band direction. Further deformation induces a multiplication of shear bands whose propagation is hindered by the dendrites. Three mechanisms are possible for the

shear bands to overcome these obstacles[24,33]: (i) they are stopped, (ii) they move around the dendrites, (iii) they cut through the dendrites. The second mechanism usually occurs at the first stage of deformation, whereas the third one is more likely to happen when a higher amount of strain is achieved. In all the cases, the propagation of the shear bands is delayed, which, macroscopically, results in an enhanced ductility. The intrinsic deformation behavior of the dendrites via dislocation slip and multiplication also contributes to the work-hardening and to the plastic deformability of the material. In the Zr-Ti-Ni alloy with hcp dendrites, deformation-induced twinning of the α-Zr dendritic phase is also supposed to help the material to sustain plastic deformation[27].

5.2. Nanoeutectic structure

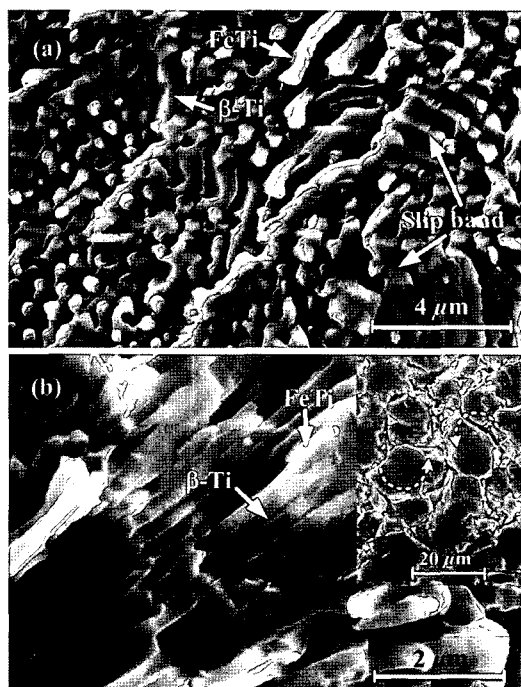The fracture surfaces of the $Ti_{70.5}Fe_{29.5}$ and $Ti_{67.79}Fe_{28.36}Sn_{3.85}$ alloys are shown in Fig. 10(a) and

Fig. 10. SEM micrographs of the fracture surface of the $Ti_{70.5}Fe_{29.5}$ (a) and $Ti_{67.79}Fe_{28.36}Sn_{3.85}$ (b) alloys. The inset in (b) shows the rotation of the eutectic colonies due to interaction with the shear bands.

(b) respectively[28]. For both alloys, slip traces are detected at the β-Ti (A2)/FeTi (B2) interface. For the binary alloy, the fracture surface reveals pronounced delamination and cutting of the FeTi rods. For the ternary alloy, a change from the rod shape to a plate shape of the FeTi phase as well as a decrease in the thickness of the β-Ti phase are observed. Rotation of the eutectic colonies (inset of Fig. 10(b)) indicates accommodation of the shear strain at the interface.

The ductility of the eutectic structure is supposed to be controlled by the compatibility between the A2 and B2 interface. During deformation, dislocations emitted from the β-Ti phase pile up at the A2/B2 interface. In order to relax the stress concentration at the tip of the pile-up, slip transfer occurs. Dislocations are absorbed at the interface and decompose by emitting a dislocation in the FeTi phase. The fracture surface of the binary alloy suggests that the stress required to activate slip in the FeTi phase is higher than the one to initiate cleavage, leading to a low macroscopic ductility[37,38]. On the contrary, in the ternary alloy, because of Sn addition, a higher lattice mismatch between the A2 and B2 exists and helps to absorb the dislocation emitted in the β-Ti phase during deformation. Slip transfer to the FeTi phase occurs and leads to an enhanced macroscopic ductility[28].

6. Summary and Outlook

A new class of nanostructured materials and their composites has been prepared by using an *in-situ* processing method. The nanotructured matrix/dendrites composites exhibit improved mechanical properties with a high strength (> 1 GPa) and an enhanced plastic deformation (up to 30%). The deformation behavior of the composite structures can be tailored by adopting the proper processing route and alloy composition and a large variety of strength-ductility combinations can be achieved. However, the presence of a ductile phase is not mandatory to reach a significant ductility. We have shown that refinement of the eutectic structure in a Ti-base alloy leads to a high strength associated with enhanced plastic deformability up to 9.6%.

Acknowledgements

References

1. H. Gleiter: Acta Mater. **48** (2000) 1.
2. A. Inoue: Acta Mater. **48** (2000) 279.
3. C. Suryanarayana: Int. Met. Rev. **40** (1995) 41.
4. C.C. Koch and T.R. Malow: Mater. Sci. Forum **312-314** (1999) 565.
5. E. Ma: Scripta Mater. **49** (2003) 663.
6. Y. Champion, C. Langlois, S. Guérin-Mailly, P. Langlois, J.L. Bonnentien and M.J. Hÿtch: Science **300** (2003) 310.
7. Q. Wei, D. Jia, K.T. Ramesh and E. Ma: Appl. Phys. Lett. **81** (2002) 1240.
8. M. Legros, B.R. Elliott, M.N. Rittner, J.R. Weertman and K.J. Hemker: Phil. Mag. A **80** (2000) 1017.
9. E. Ma: JOM **58** (2006) 49.
10. Y.M. Wang and E. Ma: Acta Mater. **52** (2004) 1699.
11. L. Lu, R. Schwaiger, Z.W. Shan, M. Dao, K. Lu and S. Suresh: Acta Mater. **53** (2005) 2169.
12. H. Choi-Yim, R. Busch, U. Köster and W.L. Johnson: Acta Mater. **47** (1999) 2455.
13. S. Deledda, J. Eckert and L. Schultz: Scripta Mater. **46** (2002) 31.
14. S. Billard, J.P. Fondère, B. Bacroix and G.F. Dirras: Acta Mater. **54** (2006) 411.
15. Y.M. Wang, M. Chen, F. Zhou and E. Ma: Nature **419** (2002) 912.
16. G He, J. Eckert, W. Löser and L. Schultz: Nature Mater. **2** (2003) 33.
17. Q.L. Dai, B.B. Sun, M.L. Sui, G He, Y. Li, J. Eckert, W.K. Luo and E. Ma: J. Mater. Res. **19** (2004) 2557.

18. U. Kühn, J. Eckert, N. Mattern and L. Schultz: Appl. Phys. Lett. **80** (2002) 2478.

19. J. Eckert, U. Kühn, N. Mattern, G. He and A. Gebert: Intermetallics **10** (2002) 1183.

20. C.C. Hays, C.P. Kim and W.L. Johnson: Phys. Rev. Lett. **84** (2000) 2901.

21. J. Eckert, J. Das and K.B. Kim: *Nanostructured composites: Ti-base alloys*. Marcel Dekker, NY, USA ed. Encyclopedia of Nanoscience and Nanotechnology. 2006. 40.

22. J. Eckert, U. Kühn, J. Das, S. Scudino and N. Radtke: Adv. Eng. Mater. **7** (2005) 587.

23 G. He, J. Eckert, W. Löser and M. Hagiwara: Acta Mater. **52** (2004) 3035.

24. G. He and W. Löser, Eckert: J. Acta Mater. **51** (2003) 5223.

25. J. Das, A. Güth, H.J. Klauß, C. Mickel, W. Löser, J. Eckert, S.K. Roy and L. Schultz: Scripta Mater. **49** (2003) 1189.

26. J. Das, W. Löser, U. Kühn, J. Eckert, S.K. Roy and L. Schultz: Appl. Phys. Lett. **82** (2003) 4690.

27. S. Scudino, J. Das, M. Stoica, K.B. Kim, M. Kusy and J. Eckert: Appl Phys Lett **88** (2006) 201920.

28. J. Das, K.B. Kim, F. Baier, W. Löser and J. Eckert: Appl Phys Lett **87** (2005) 161907.

29. G. He, J. Eckert and W. Löser: Acta Mater. **51** (2003) 1621.

30. G. He and M. Hagiwara: Mater. Trans. JIM **45** (2004) 1555.

31. Z.F. Zhang, G. He, H.F. Zhang and J. Eckert: Scripta Mater. **52** (2005) 945.

32. Z.F. Zhang, J. Eckert and L. Schultz: Phys. Rev. Lett. **91** (2003) 045505.

33. J. Eckert, J. Das, K.B. Kim, F. Baier, W. Löser, M. Calin, Z.F. Zhang and A. Gebert: J Alloy Comp 2006 (accepted).

34. K.B. Kim, J. Das, F. Baier and J. Eckert: Phys. Stat. Sol. a **202** (2005) 2405.

35. K.B. Kim, J. Das, F. Baier and J. Eckert: Appl Phys Lett **86** (2005) 201909.

36. K.B. Kim, J. Das, F. Baier and J. Eckert: Appl Phys Lett 86 (2005) 171909.

37. J. Das, K.B. Kim, W. Xu, W. Löser and J. Eckert: Mater Sci Eng A 2006 (In press).

38. J. Das, K.B. Kim, F. Baier, W. Löser, A. Gebert and J. Eckert: J. Alloy Comp 2006 (In press).